REPORT

PHYSICS

Magnetic resonance spectroscopy of an atomically thin material using a single-spin qubit

I. Lovchinsky,[1] J. D. Sanchez-Yamagishi,[1,2] E. K. Urbach,[1] S. Choi,[1] S. Fang,[1] T. I. Andersen,[1] K. Watanabe,[4] T. Taniguchi,[4] A. Bylinskii,[1,2] E. Kaxiras,[1,3] P. Kim,[1] H. Park,[1,2,5]* M. D. Lukin[1]*

Two-dimensional (2D) materials offer a promising platform for exploring condensed matter phenomena and developing technological applications. However, the reduction of material dimensions to the atomic scale poses a challenge for traditional measurement and interfacing techniques that typically couple to macroscopic observables. We demonstrate a method for probing the properties of 2D materials via nanometer-scale nuclear quadrupole resonance (NQR) spectroscopy using individual atomlike impurities in diamond. Coherent manipulation of shallow nitrogen-vacancy (NV) color centers enables the probing of nanoscale ensembles down to approximately 30 nuclear spins in atomically thin hexagonal boron nitride (h-BN). The characterization of low-dimensional nanoscale materials could enable the development of new quantum hybrid systems, combining atomlike systems coherently coupled with individual atoms in 2D materials.

Hexagonal boron nitride (h-BN) is an insulating material consisting of equal concentrations of boron (80% ^{11}B, 20% ^{10}B) and nitrogen (close to 100% ^{14}N) in a honeycomb layered structure (*1*). The individual atomic layers of h-BN are held together by weak van der Waals interactions, allowing the preparation of samples with varying numbers of layers via mechanical exfoliation (*2*). Nanometer-thick h-BN flakes are being extensively used as dielectric spacers and passivation layers for graphene and transition metal dichalcogenides (*1*, *3*). Recent studies have shown that atomically thin h-BN can be the host for interesting quantum defects (*4*). We investigate both the electron density distribution and spin-spin interactions in nanoscale h-BN volumes by analyzing the magnetic fields produced by ^{11}B, ^{10}B, and ^{14}N spins using nanoscale nuclear quadrupole resonance (NQR) spectroscopy (*5*, *6*).

Conventional NQR spectroscopy is a powerful tool for chemical analysis that relies on detecting the bulk magnetization of quadrupolar ($I > 1/2$) nuclear spins in a weak magnetic field (*7*, *8*). The NQR spectrum is determined by the interaction between the nuclear electric quadrupole moments and the local electric field gradients (*9*) and is thus dependent on the electrostatic environment of the measured spins. In the case when the target material is axially symmetric and no external magnetic field is applied, the quadrupolar interaction defines a principal axis for the nuclear spins. For the special case of $I = 3/2$, application of a small magnetic field yields a set of perturbed spin eigenstates, with energies that depend on the orientation of the applied field with respect to the principal axis (Fig. 1B). NQR spectroscopy yields the transition frequencies and relaxation/decoherence rates, which in turn can be related to various material properties (*10*, *11*) (e.g., chemical composition, bond lengths, and angles). However, conventional magnetic resonance methods require macroscopic samples (*12*) and are not suitable for experiments with atomically thin layers.

In our approach, individual NV centers in diamond are used as sensitive, atomic-scale magnetic field sensors to probe nanoscale h-BN samples under ambient conditions (*5*, *6*, *13*, *14*). Formed using ion implantation within several nanometers from the diamond surface, NV centers can have sensing volumes that are many orders of magnitude smaller than most conventional magnetic sensing techniques (*2*, *15*). In our experiments, a target h-BN flake is transferred onto the surface of a diamond (*2*), and a proximal NV center is used to detect NQR signals from small ensembles of nuclear spins within the h-BN crystal (Fig. 1A). Importantly, the coherence properties of the NV spin are not affected by the presence of the h-BN flake, indicating that the generation of a new quantum interface between a two-dimensional (2D) material and diamond is feasible. To use the NV center as a nanoscale NQR spectrometer, the NV electronic spin state is prepared in a coherent superposition of the magnetic sublevels $m_s = 0$ and $m_s = 1$ and is periodically modulated with k microwave (MW) π pulses using a modified XY8-k pulse sequence [see Fig. 1C and (*2*)]. When the local magnetic field spectrum contains a Fourier component near half of the modulation frequency, the NV spin state accumulates a net phase (resulting in a measurable population signal) while components at other frequencies are efficiently cancelled (*16*). Repetition of this sequence at different modulation frequencies yields the NQR spectrum. Whereas conventional NQR spectroscopy suffers from poor sensitivity due to low thermal polarization under small magnetic field (*10*), our method relies on measuring the statistical fluctuations of the spin polarization (proportional to $\sqrt{N}$, where N is the number of nuclear spins in the sensing volume), which is independent of the applied field. In the limit of small N, the statistical polarization can be much larger than the thermal polarization, resulting in effective polarizations as high as ~3%.

In the ^{11}B ($I = 3/2$) NQR spectrum of a ~30-nm-thick h-BN flake, measured using an XY8-371 sequence (Fig. 2A), the resonance frequencies are determined by the quadrupole coupling constant $\overline{Q}$, which is the product of the scalar nuclear electric quadrupole moment and the largest eigenvalue of the local electric field gradient tensor (*9*). The extracted $\overline{Q} = 2.9221 \pm 0.0006$ MHz is in excellent agreement with values measured in macroscopic NQR experiments (2.96 ± 0.10 MHz) (*17*). The effective sensing volume is determined by the depth of the NV center (6.8 ± 0.1 nm) and corresponds to ~20 atomic layers of h-BN material (*2*). The external magnetic field (~30 G) is applied parallel to the NV symmetry axis, which forms a 54.7° angle with the surface normal. In this configuration (Fig. 1B), the frequencies of the central transitions ($|m_I = \pm 1/2\rangle \rightarrow |\pm 3/2\rangle$) are degenerate, whereas the satellite peaks, corresponding to dipole-forbidden $|\mp 1/2\rangle \rightarrow |\pm 3/2\rangle$ transitions, become weakly allowed due to mixing by the magnetic field component perpendicular to the h-BN principal axis. Rotation of the polar angle of the magnetic field away from the NV axis lifts the degeneracy of the central transitions (Fig. 2D), in excellent agreement with theoretical prediction (Fig. 2E). Figure 2, B and C, shows that when the magnetic field is increased so that the Zeeman and quadrupolar interactions are of the same order, the NQR spectrum becomes very sensitive to the magnetic field angle (sensitivity is ~80 kHz/degree at ~1700 G), enabling precise measurement of the h-BN crystal orientation (in our case perpendicular to the interface).

Measurement of the spectral shifts and linewidths sheds light on the dynamics and interactions governing the nuclear spins. Figure 3A shows the $|+1/2\rangle \rightarrow |-3/2\rangle$ ^{11}B NQR resonance alongside an externally applied calibration signal (indicated by the black arrow), whose width corresponds to the Fourier limit, determined by the

[1]Department of Physics, Harvard University, Cambridge, MA 02138, USA. [2]Department of Chemistry and Chemical Biology, Harvard University, Cambridge, MA 02138, USA. [3]John A. Paulson School of Engineering and Applied Sciences, Harvard University, Cambridge, MA 02138, USA. [4]National Institute for Materials Science, Tsukuba, Japan. [5]Broad Institute of MIT and Harvard, 7 Cambridge Center, Cambridge, MA 02142, USA.
*Corresponding author. Email: lukin@physics.harvard.edu (M.D.L.); hongkun_park@harvard.edu (H.P.)

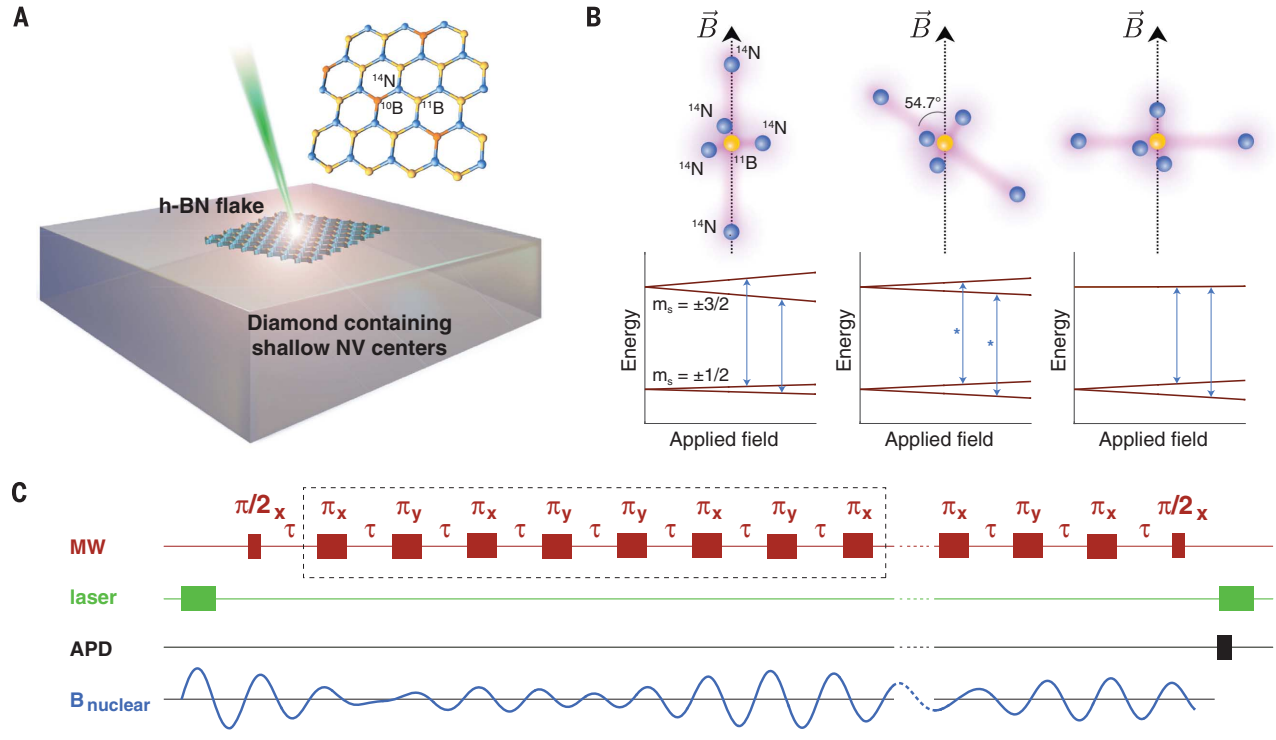

Fig. 1. Experimental setup and sensing scheme. (**A**) Schematic of experimental setup. The h-BN flake (structure shown on top) is transferred onto a diamond surface. A proximal shallow NV center is used to detect nuclear spins within the h-BN crystal. (**B**) The dependence of the level structure of a quadrupolar nuclear spin on a small applied magnetic field. The three configurations shown correspond to a spin-3/2 object where the external magnetic field is applied parallel, at a 54.7° angle and perpendicular to the principal axis. The central transitions are shown by blue arrows. In the middle configuration, the center transitions are degenerate (indicated by *). As a specific example, these configurations are illustrated for the case of a ^{11}B spin in h-BN, surrounded by its nearest five nitrogen atoms. (**C**) NV center is subject to modified XY8-*k* pulse sequence used to measure the NQR spectrum. The unit indicated by the dashed box is repeated [see (*2*)]. APD denotes the photodetector measurement window. The magnetic field created by target nuclear spins, containing several Fourier components, is shown at the bottom.

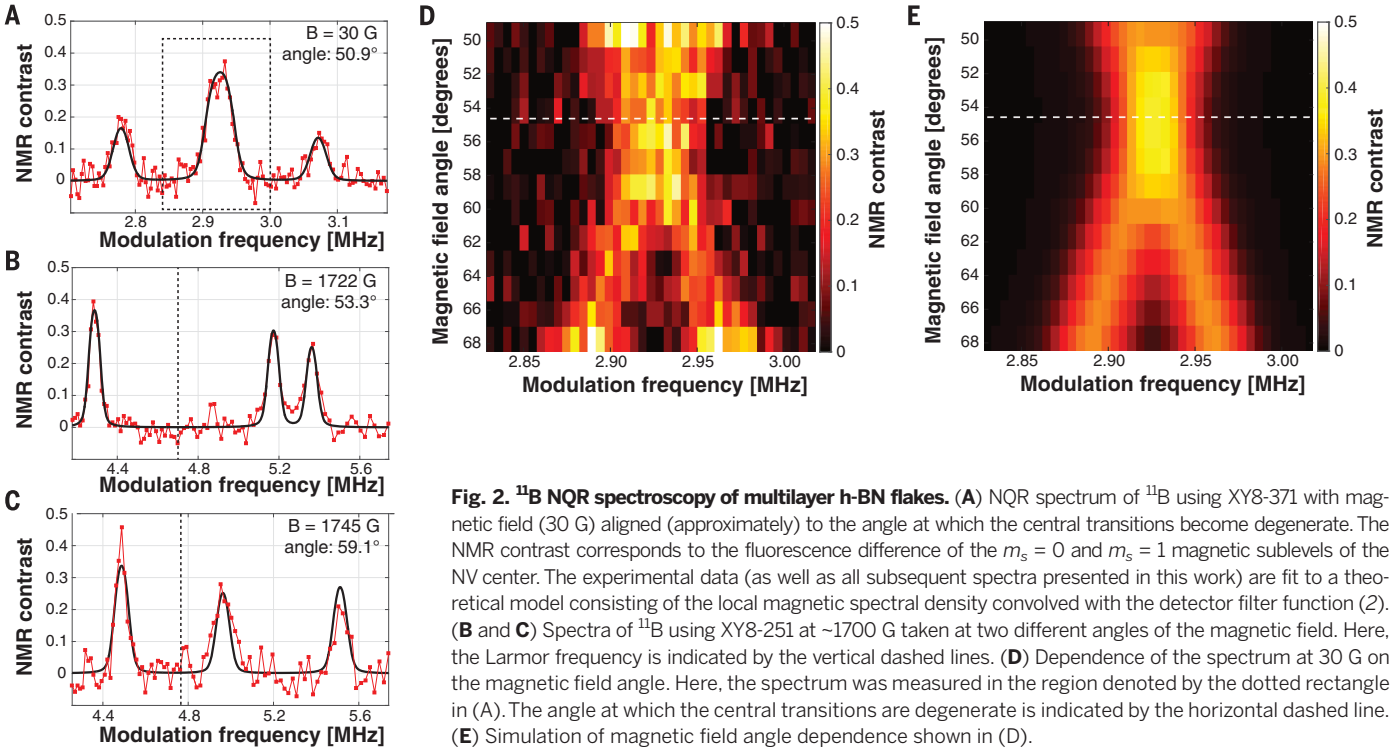

Fig. 2. ^{11}B NQR spectroscopy of multilayer h-BN flakes. (**A**) NQR spectrum of ^{11}B using XY8-371 with magnetic field (30 G) aligned (approximately) to the angle at which the central transitions become degenerate. The NMR contrast corresponds to the fluorescence difference of the $m_s = 0$ and $m_s = 1$ magnetic sublevels of the NV center. The experimental data (as well as all subsequent spectra presented in this work) are fit to a theoretical model consisting of the local magnetic spectral density convolved with the detector filter function (*2*). (**B** and **C**) Spectra of ^{11}B using XY8-251 at ~1700 G taken at two different angles of the magnetic field. Here, the Larmor frequency is indicated by the vertical dashed lines. (**D**) Dependence of the spectrum at 30 G on the magnetic field angle. Here, the spectrum was measured in the region denoted by the dotted rectangle in (A). The angle at which the central transitions are degenerate is indicated by the horizontal dashed line. (**E**) Simulation of magnetic field angle dependence shown in (D).

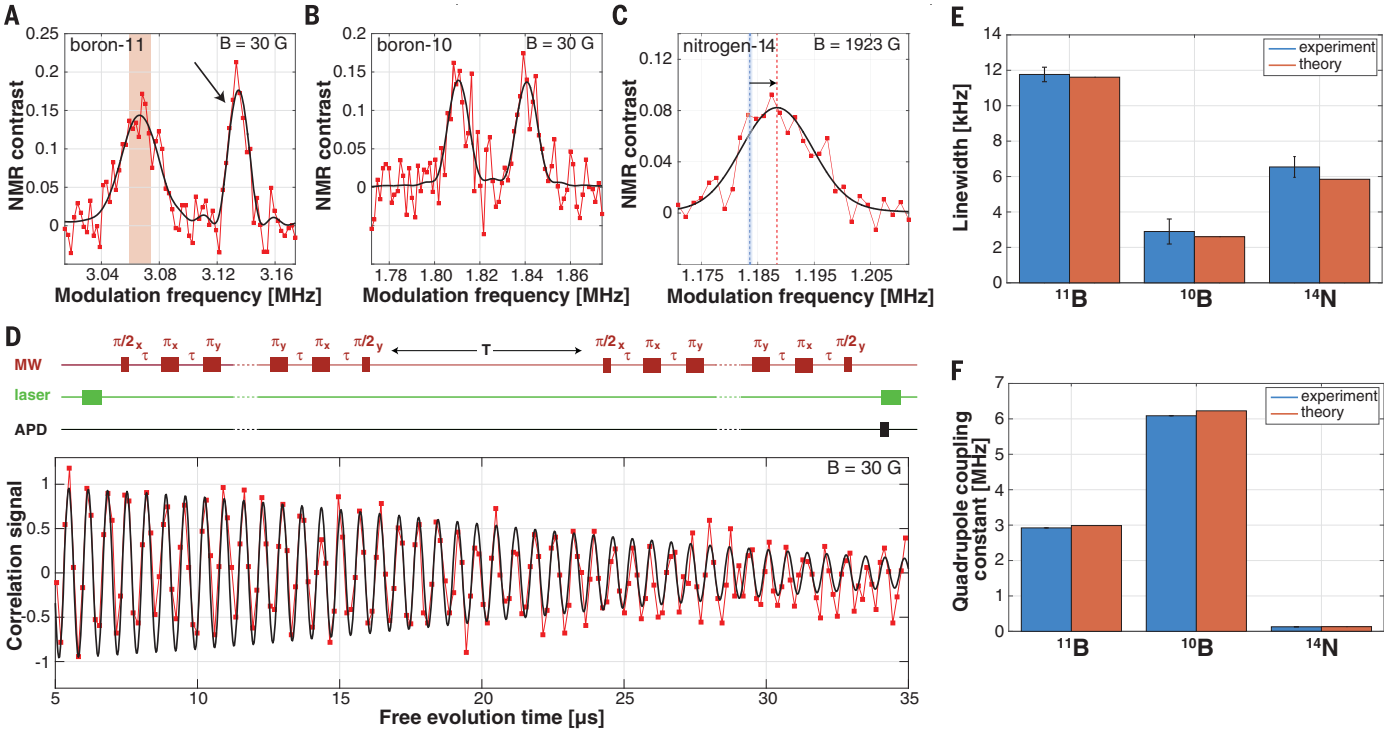

Fig. 3. NQR linewidth and quadrupole coupling constant measurements. (**A**) NQR spectrum of $|+1/2\rangle \rightarrow |-3/2\rangle$ transition of ^{11}B using XY8-371 at 30 G. A calibration signal (indicated by black arrow) is applied at frequency 1.567 MHz using an external coil. Spectral resolution of NQR signal shown by shaded region. (**B**) ^{10}B NQR spectrum using XY8-371 at 30 G. The observed spectrum corresponds (approximately) to the degenerate $|0\rangle \rightarrow |\pm1\rangle$, $|\pm1\rangle \rightarrow |\pm2\rangle$, and $|\pm2\rangle \rightarrow |\pm3\rangle$ transitions. (**C**) ^{14}N spectrum using XY8-187 taken at ~2000 G, with the field aligned to the NV symmetry axis. At this special angle, the $|0\rangle \rightarrow |\pm1\rangle$ transitions are degenerate. The quadrupole interaction is manifested as a small shift of the ^{14}N resonance (indicated by a dashed red line) relative to the Larmor frequency (indicated by a dashed blue line, with uncertainty shown by a blue band). (**D**) Pulse sequence used for time-domain measurement of linewidth (top). The result of this measurement for ^{11}B is shown at the bottom. The time trace is the free induction decay of the ^{11}B spin, where the slow decay envelope (corresponding to the nuclear spin decoherence) is modulated by fast oscillations (corresponding to the ~2.9 MHz quadrupole coupling constant). (**E**) Linewidths, measured in Fig. 3, A to D, of ^{11}B, ^{10}B, and ^{14}N (blue bars) along with simulated values (orange bars) based on dipolar coupling model (*2*). Error bars, mean ± 1 SD. (**F**) Measured quadrupole coupling constants of ^{11}B, ^{10}B, and ^{14}N (blue bars) along with theoretical values (orange bars) based on DFT. The 1-SD errors corresponding to ^{11}B, ^{10}B, and ^{14}N are 370 Hz, 1.4 kHz, and 5.9 kHz, respectively, and are too small to be visualized on the scale of this plot.

spin coherence time T_2 of the NV sensor. Deconvolution of this calibration signal from the ^{11}B resonance gives the natural NQR linewidth. A similar procedure yields the linewidth of ^{10}B ($I = 3$), where the observed doublet (Fig. 3B) corresponds to two sets of triply degenerate transitions. Figure 3C shows the ^{14}N spectrum measured at ~2000 G, where the quadrupolar interaction is manifested as a small shift from the nuclear Larmor frequency (*2*). The resonance frequencies and decoherence of NQR lines can also be measured directly (without deconvolution) in the time domain using correlation spectroscopy (*18*) (Fig. 3D, top). Here, we apply two identical pulse sequences (similar to XY8-*k*) separated by a variable free evolution interval T, which can be longer than the coherence time T_2 of the NV sensor and is limited only by the NV population relaxation time T_1. As a result, this technique yields improved spectral resolution at the expense of sensitivity (due to the additional free precession interval T). Figure 3D (bottom) shows the resulting ^{11}B time evolution, where the envelope (consistent with the linewidth measured in Fig. 3A, here modeled using a Gaussian decay) is modulated by fast oscillations (corresponding to $\overline{Q}$).

Figure 3E shows the measured ^{11}B, ^{10}B, and ^{14}N linewidths (blue bars) and the corresponding simulated linewidths (orange bars), where we assumed that the spins interact only via magnetic dipole-dipole coupling (*2*). The simulated values are in excellent agreement with our measurements, demonstrating that nanoscale volumes of h-BN constitute nearly ideal, dipolar-coupled spin systems. Figure 3F shows the measured values of $\overline{Q}$ for ^{11}B, ^{10}B, and ^{14}N (blue bars), along with calculated values (orange bars) based on density functional theory (DFT) simulations. Here, we used an all-electron model [see (*2*) for details] in the local density approximation (LDA), which yields the calculated quadrupole coupling constants within 2% of the measured values.

Figure 4A shows the ^{11}B NQR spectrum of a h-BN monolayer as compared to that of a thick (>50 nm) flake. The monolayer was characterized using Raman spectroscopy, atomic force microscopy (AFM), and second-harmonic generation microscopy [see (*2*)]. This monolayer signal corresponds to approximately $\sqrt{N} = 30$ polarized ^{11}B spins and exhibits a 17 ± 3 kHz shift of $\overline{Q}$ relative to the bulk value. Figure 4B shows the shifts of $\overline{Q}$ and the corresponding linewidths for measurements for several NV centers under a monolayer flake (red) and a bilayer flake (green), as compared to measurements on several thick layers (blue). We find that the bilayer shifts are in between the monolayer and bulk values, and the signals for all the NV centers in both the monolayer and bilayer configurations shift in a consistent manner.

The origin of the $\overline{Q}$ shifts can be understood qualitatively by considering the reduction of the dimensionality of the h-BN crystal. As the number of layers in the crystal is reduced, we expect that the electric field gradient experienced by a nuclear spin will deviate from its bulk value. A toy model in which in-plane sp^2 bonding electrons are modeled as point charges placed at interstitial sites between the boron and nitrogen ions yields an electric field gradient shift in the correct direction, although the magnitude is smaller by a factor of ~20 than the observed value (*2*). To study this effect quantitatively, we performed DFT simulations of the electric field

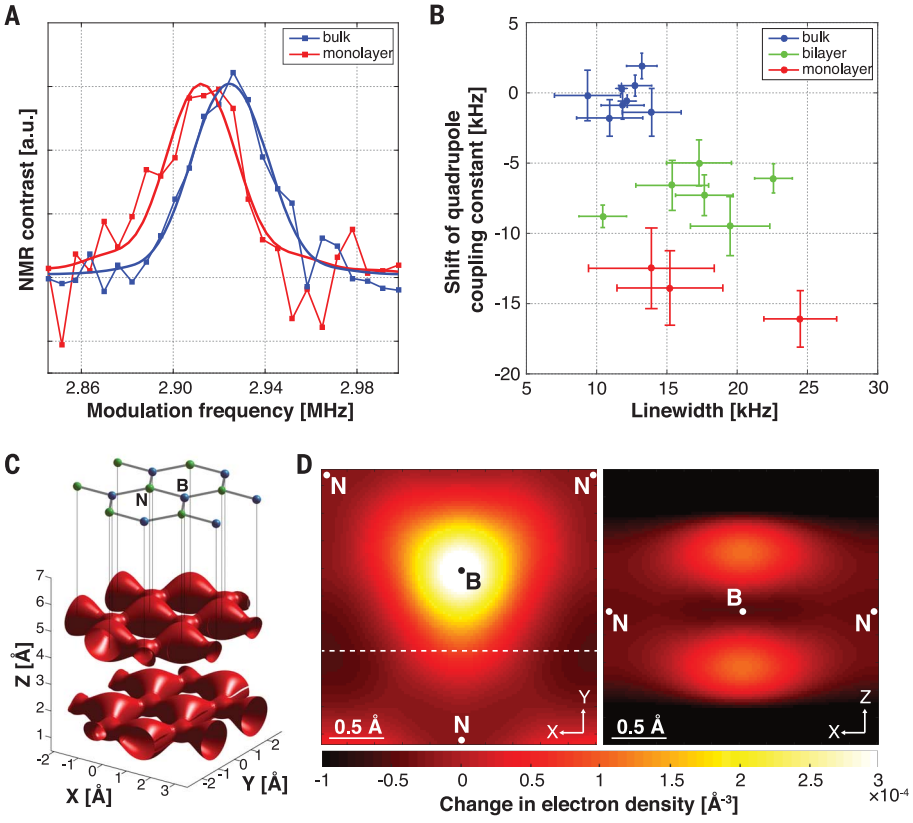

Fig. 4. NQR spectroscopy of a h-BN monolayer and bilayer. (**A**) ^{11}B NQR spectrum using XY8-187 of thick (greater than 50 nm) h-BN flake (blue) as compared to a monolayer (red). Magnetic field is aligned with respect to NV symmetry axis. Spectra have been normalized so that the resonances have the same magnitude, for comparison. The integration time for the monolayer data was about 1 day, or 1 hour per data point. (**B**) Values of the shift of $\overline{Q}$ and deconvolved linewidths for several NV centers under a monolayer flake (red), a bilayer flake (green), and five bulk flakes (blue). Error bars, mean ± 1 SD. (**C**) Visualization of electron density for two layers of bulk h-BN, as calculated with DFT. A single contour, corresponding to a density of ~1 Å^{-3}, is shown. Boron and nitrogen sites are indicated in the schematic of atomic structure (top). (**D**) (Left) Visualization of the excess electron caps in the *x*/*y* plane (0.8 Å above the atom plane). A single unit cell is shown. The image corresponds to the difference between the monolayer and bulk electron densities. (Right) Visualization of the excess electron caps in the *x*/*z* plane (*y* value indicated by dashed line in left panel). Projected positions of boron and nitrogen ions are indicated.

gradient in the monolayer, bilayer, and bulk configurations (*2*). These simulations indeed show that reducing the number of layers in the crystal shifts $\overline{Q}$ to lower frequencies. We find that the calculated shifts (–15 kHz for bilayer, –25 kHz for monolayer) are within 50% of the measured values. Remarkably, DFT calculations show that the contribution to the electric field gradient shift resulting from the removal of the outer layers (and their associated charges) accounts for only ~20% of the shift. The dominant contribution arises from a partial redistribution of the electron density (at the level of 10^{-4} of an elementary charge) from its bulk configuration (see Fig. 4C) into a pair of negative charge "caps" above and below boron in the monolayer configuration (Fig. 4D). The additional broadening observed in some of the monolayer and bilayer spectra is likely due to dipolar interactions with proximal ^{1}H spins contained within the polycarbonate stamp, as well as in the ubiquitous proton layer at the diamond surface, associated with adsorbed hydrocarbons [see (*19*) and (*2*), where we probe this layer directly via proton nuclear magnetic resonance (^{1}H NMR)]. In addition to changes in the electrostatic and magnetic environment due to the reduction in layers, differences in lattice strain between the bulk and 2D configurations or the presence of the diamond and polycarbonate substrates may also contribute to shifts and broadening.

These observations provide new insight into the local properties of 2D materials. The sensitivity and spectral resolution can be improved using spin-to-charge conversion readout (*20*) and advanced photonic structures for improved collection efficiency. With these improvements, individual ^{11}B spins can be detected within 1 second of integration time (*2*). The use of correlation spectroscopy (Fig. 3D) provides a way of extending the sensing time beyond the coherence time of the NV center. Combined with advanced nuclear decoupling pulse sequences (*21*) and modest cooling of the diamond samples to ~100 K (*22*), this method can be used to improve the spectral resolution down to the level of ~1 Hz. Scanning diamond tips (*23*) or optical super-resolution techniques (*24*) can be used for nanoscale imaging of local strain fields, localized defects, piezoelectric properties, and crystallinity in nanoscale materials (*3*, *25*, *26*).

In addition to providing a new sensing modality, our approach can be used to observe and coherently control dynamics of individual nuclear spins in 2D materials. In particular, NV centers can be used as actuators to coherently control nuclear spins in 2D materials (*27*–*29*). Nuclear spin polarization and control can be achieved by selectively pumping individual quanta of polarization from the NV center to the desired nuclear spin via Hartmann-Hahn double resonance (*27*, *30*), whereas interactions among nuclear spins can be engineered via pulsed radio frequency control (*28*). Our experiments show that nuclear dynamics in 2D materials can be limited by dipole-dipole interactions [the additional broadening observed in some of our measurements can likely be controlled by removing proton spins from the diamond surface (*5*)]. Such a coherently coupled system can be used as a novel hybrid platform for quantum information processing (*28*) and for studying quantum dynamics of isolated strongly interacting nuclear spin systems (*31*).

REFERENCES AND NOTES

1. K. S. Novoselov, A. Mishchenko, A. Carvalho, A. H. Castro Neto, *Science* **353**, aac9439 (2016).
2. Materials, methods, and supplementary online text are available as supplementary materials.
3. A. K. Geim, I. V. Grigorieva, *Nature* **499**, 419–425 (2013).
4. T. T. Tran, K. Bray, M. J. Ford, M. Toth, I. Aharonovich, *Nat. Nanotechnol.* **11**, 37–41 (2016).
5. T. Staudacher *et al.*, *Science* **339**, 561–563 (2013).
6. H. J. Mamin *et al.*, *Science* **339**, 557–560 (2013).
7. T. P. Das, E. L. Hahn, *Nuclear Quadrupole Resonance Spectroscopy* (Academic Press Publishers, New York, 1958).
8. D. B. Zax, A. Bielecki, K. W. Zilm, A. Pines, D. P. Weitekamp, *J. Chem. Phys.* **83**, 4877–4905 (1985).
9. B. H. Suits, *Handbook of Applied Solid State Spectroscopy* (Springer, New York, USA, 2006).
10. U. Werner, B. Black, M. Ziegeweid, A. Pines, *Chem. Phys. Lett.* **209**, 17–21 (1993).
11. S. Brummer, A. Weiss, *Ber. Bunsenges. Phys. Chem* **94**, 497–513 (1990).
12. P. Glover, S. P. Mansfield, *Rep. Prog. Phys.* **65**, 1489–1511 (2002).
13. J. R. Maze *et al.*, *Nature* **455**, 644–647 (2008).
14. I. Lovchinsky *et al.*, *Science* **351**, 836–841 (2016).
15. T. Wolf *et al.*, *Phys. Rev. X* **5**, 041001 (2015).
16. L. M. Pham *et al.*, *Phys. Rev. B* **93**, 045425 (2016).
17. A. H. Silver, P. J. Bray, *J. Chem. Phys.* **32**, 288–292 (1960).
18. T. Staudacher *et al.*, *Nat. Commun.* **6**, 8527 (2015).
19. S. J. DeVience *et al.*, *Nat. Nanotechnol.* **10**, 129–134 (2015).
20. B. J. Shields, Q. P. Unterreithmeier, N. P. de Leon, H. Park, M. D. Lukin, *Phys. Rev. Lett.* **114**, 136402 (2015).
21. P. C. Maurer *et al.*, *Science* **336**, 1283–1286 (2012).
22. A. Jarmola, V. M. Acosta, K. Jensen, S. Chemerisov, D. Budker, *Phys. Rev. Lett.* **108**, 197601 (2012).
23. P. Maletinsky *et al.*, *Nat. Nanotechnol.* **7**, 320–324 (2012).
24. T. Klar, R. Wollhofen, J. Jacak, *Phys. Scr.* **T162**, 014049 (2014).
25. M. Chhowalla, Z. Liu, H. Zhang, *Chem. Soc. Rev.* **44**, 2584–2586 (2015).
26. M. P. Boneschanscher *et al.*, *Science* **344**, 1377–1380 (2014).
27. C. D. Aiello, P. Cappellaro, *Phys. Rev. A* **91**, 042340 (2015).
28. J. Cai, A. Retzker, F. Jelezko, M. B. Plenio, *Nat. Phys.* **9**, 168–173 (2013).

29. S. Kolkowitz, Q. P. Unterreithmeier, S. D. Bennett, M. D. Lukin, *Phys. Rev. Lett.* **109**, 137601 (2012).
30. P. London *et al.*, *Phys. Rev. Lett.* **111**, 067601 (2013).
31. J. W. Britton *et al.*, *Nature* **484**, 489–492 (2012).

ACKNOWLEDGMENTS

The authors thank R. Walsworth, F. Casola, B. Dwyer, N. de Leon, O. Grånäs, and S. Carr for many helpful discussions and experimental help. This work was supported by the Defense Advanced Research Projects Agency (QuASAR program), National Science Foundation (NSF), Center for Ultracold Atoms, Army Research Office (ARO) MURI program, National Security Science and Engineering Faculty Fellowship program, and Moore Foundation. S.F. was supported by the STC Center for Integrated Quantum Materials, NSF grant DMR-1231319. E.K.U. acknowledges support by the NSF (Graduate Research Fellowship Program under grant DGE1144152). S.C. acknowledges support from the Kwanjeong Educational Foundation. E.K. acknowledges support from ARO MURI award W911NF-14-0247. This work used the Extreme Science and Engineering Discovery Environment (XSEDE), which is supported by NSF grant ACI-1053575. K.W. and T.T. acknowledge support from the Elemental Strategy Initiative conducted by MEXT, Japan, and JSPS KAKENHI grants JP26248061, JP15K21722, and JP25106006.

SUPPLEMENTARY MATERIALS

www.sciencemag.org/content/355/6324/503/suppl/DC1
Materials and Methods
Supplementary Text
Figs. S1 to S4
References (*32*–*48*)

20 October 2016; accepted 6 January 2017
Published online 19 January 2017
10.1126/science.aal2538